Article

Investigating the Effects of Copper Impurity Deposition on the Structure and Electrochemical Behavior of Hydrogen Evolution Electrocatalyst Materials

Sonakshi Saini, Salem C. Wright, Sahanaz Parvin, Jonas Baltrusaitis, and Matthew T. McDowell*

Read Online

ACCESS | Metrics & More | Article Recommendations | SI Supporting Information

ABSTRACT: Electrolysis of impure water (such as seawater) has recently garnered research interest as it may enable hydrogen production at reduced costs. However, the tendency of impurity ions and other species to degrade electrocatalysts and membranes within an electrolyzer is a serious challenge. Here, we investigate the effects of copper impurities of varying concentrations on the hydrogen evolution reaction (HER) using platinum electrocatalysts. A decrease of current density is observed with an increasing copper concentration. By comparing the effect of ionic impurities on current density at different concentrations, we gain insight into how impurities can interfere with the HER at different potentials. Surface characterization of the electrodes reveals differences in the morphology and extent of copper deposition on HER-active platinum vs inactive gold electrodes. This enables an improved understanding of how copper nucleates and grows on the two types of electrodes under different electrochemical conditions while also confirming deposition in low-concentration cases, as present in seawater. The results indicate that copper electrodeposition competes with the HER, and the nature of copper electrodeposition varies depending on the electrocatalytic activity of the electrode. This study provides insight toward catalyst design that can withstand the effects of impurity-induced degradation over extended use.

KEYWORDS: hydrogen evolution electrocatalysts, seawater splitting, copper impurities, platinum, morphology evolution
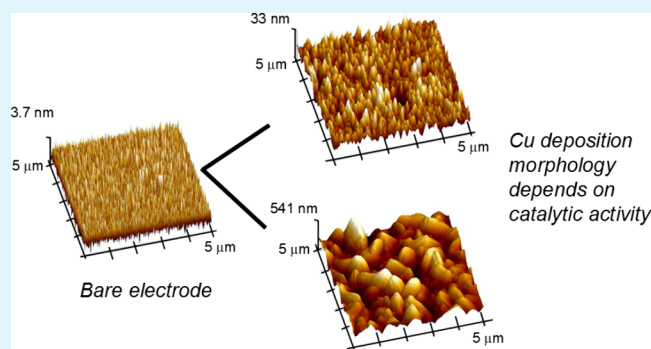
INTRODUCTION

Hydrogen is a sustainable alternative to fossil fuels due to its versatility as an energy carrier for transportation and grid storage.[1−6] Electrolysis of water to form hydrogen and oxygen can be used to produce hydrogen with renewable electricity.[7−10] While electrolysis is a well-known process, there are several limitations hindering efficient and cost-effective hydrogen production.[11−13]

One limitation of hydrogen production is that commercial electrolyzers require ultrapure water,[14,15] and purification involves significant capital investment and is energy intensive. Investigation of direct seawater splitting has been carried out recently to potentially reduce the cost of hydrogen production.[16−20] Much work has focused on electrolyzers, with work on membranes[21−23] and electrocatalysts[24−30] for the direct electrolysis of seawater. However, the practicality of seawater splitting is disputed due to the associated complications.[31] Ionic or organic impurities naturally present in seawater can impact electrolyzer operation by reacting with or deactivating various components.[32,33] This effect is particularly damaging to the membranes[34−39] and electrocatalysts.[40−44] Impurities can severely degrade catalytic activity by occupying active sites and poisoning the catalyst surface,

rendering these sites unavailable for binding to reaction intermediates.[45−47]

At the positive electrode in an electrolyzer, oxidation of anions such as chloride[21,48,49] and bromide[50,51] can compete with the oxygen evolution reaction (OER), which can affect the catalytic selectivity toward OER.[52,53] For the hydrogen evolution reaction (HER) at the negative electrode, platinum (Pt) is usually regarded as the ideal electrocatalyst,[54−56] and it has been the primary focus of electrocatalyst design for water electrolysis.[57,58] However, metal ion impurities within the electrolyte that exhibit a reduction potential within the range of HER can deposit on the electrocatalyst, affecting the HER efficiency[41,44,59] and thus influencing the operation of the electrolyzer. Underpotential deposition of different metals on Pt has been widely studied, highlighting metal ion impurities
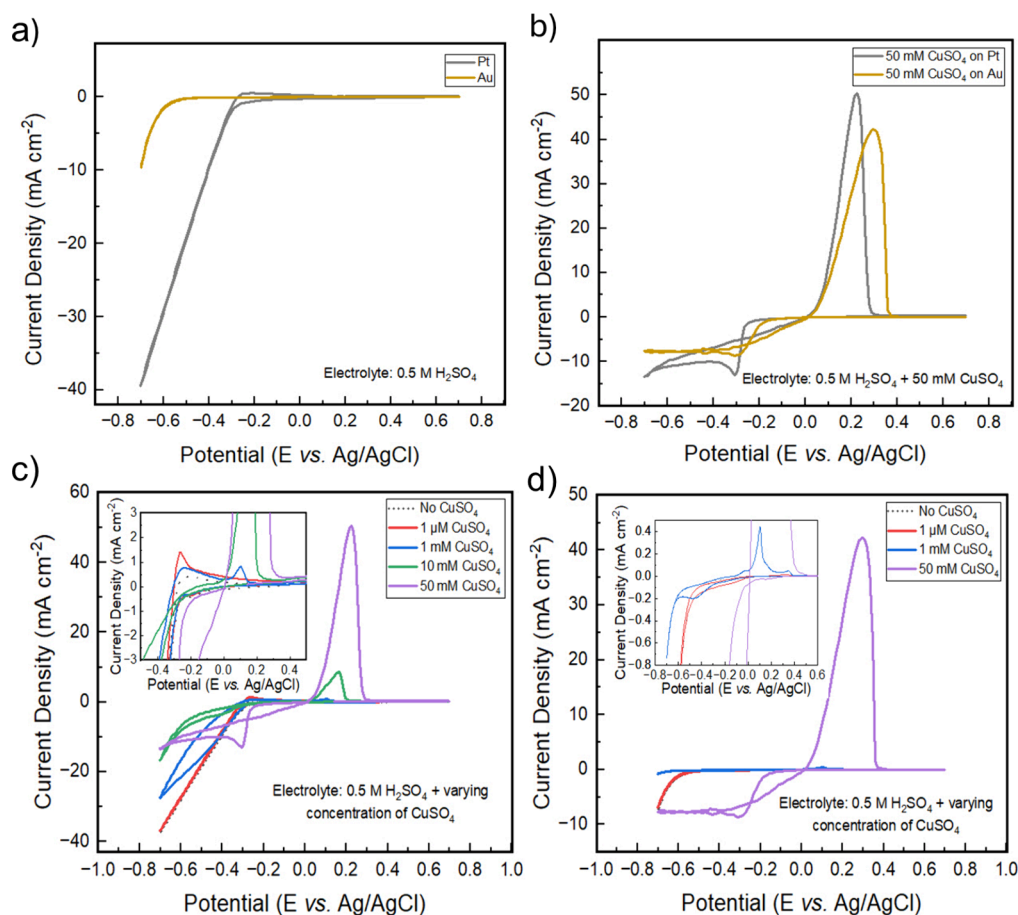
Figure 1. (a) CV tests of Pt and Au electrodes in 0.5 M H$_2$SO$_4$ electrolyte. (b) Fifth-cycle CV tests of Pt and Au electrodes in 0.5 M H$_2$SO$_4$ + 50 mM CuSO$_4$ electrolyte. (c) Fifth-cycle CV tests of Pt electrodes in 0.5 M H$_2$SO$_4$ (dotted black), 0.5 M H$_2$SO$_4$ + 1 μM CuSO$_4$ (red), 0.5 M H$_2$SO$_4$ + 1 mM CuSO$_4$ (blue), 0.5 M H$_2$SO$_4$ + 10 mM CuSO$_4$ (green), and 0.5 M H$_2$SO$_4$ + 50 mM CuSO$_4$ (purple), with magnified inset to show the oxidation peak for 1 mM CuSO$_4$. (d) Fifth-cycle CV tests of Au electrodes in 0.5 M H$_2$SO$_4$ (dotted black), 0.5 M H$_2$SO$_4$ + 1 μM CuSO$_4$ (red), 0.5 M H$_2$SO$_4$ + 1 mM CuSO$_4$ (blue), and 0.5 M H$_2$SO$_4$ + 50 mM CuSO$_4$ (purple), with magnified inset to show the curve for 1 mM CuSO$_4$.

that can potentially affect the efficiency of HER,[60] along with comparisons to other electrocatalyst materials.[61]

Copper (Cu) ions warrant investigation as a prototypical impurity since their reduction potential is near the HER potential (0.34 V vs SHE for Cu^{2+}/Cu and 0.15 V vs SHE for Cu^{2+}/Cu$^+$), and this ion is also found in seawater in concentrations ranging from 0.01 μM to greater than 3 μM due to industrial contamination.[62,63] It has been well-documented that underpotential deposition of Cu affects HER,[64,65] but there is a limited understanding of how the electrodeposition of Cu influences electrocatalyst evolution and HER characteristics. In particular, understanding how the dynamic deposition of Cu from electrolytes with different concentrations influences the HER on various electrocatalyst materials is needed. This information may further be used to understand the effect of other ionic impurities on electrolyzer behavior.

Here, we investigate the effect of Cu ionic impurities on HER in an acidic environment using Pt electrodes, and we contrast this behavior with gold (Au) electrodes. These materials represent both electrocatalytic and nonelectrocatalytic systems.[41,66,67] This study thus aims to understand how impurities interact with different metallic electrodes with different levels of electrocatalytic activity. An acidic environment is used to isolate the effects of Cu impurities to fully understand their effects on the HER without interfering effects

of pH gradients or other species. We study the effects of varying Cu concentration to understand electrochemical competition between Cu electrodeposition and the HER. Scanning electron microscopy (SEM), atomic force microscopy (AFM), and X-ray photoelectron spectroscopy (XPS) are used to investigate the morphology and chemistry of the electrode surfaces after operating under different electrochemical conditions. The results show a decreasing trend of current density with increasing Cu concentration, which indicates that the presence of Cu ions suppresses HER, resulting in a concentration-dependent trade-off between HER and Cu electrodeposition. Surface characterization reveals differences in the shape and morphology of Cu deposits on Au and Pt, suggesting that HER influences the nature of electrodeposition. Furthermore, Cu deposition is observed at all considered concentrations (including at the relatively low concentrations of Cu in seawater). This work highlights the competition between impurity deposition and HER, as well as the importance of understanding and controlling impurity effects in electrolysis.

■ EXPERIMENTAL METHODS

Working Electrode Preparation. To prepare the working electrodes, Au or Pt was deposited (100 nm, with a 10 nm thick Ti adhesion layer) on heat-treated (800 °C) silicon wafers (n-type, Wafer Works Corp.) via a Denton Explorer e-beam evaporator

system. The wafers were then scribed to obtain smaller samples to make electrodes. A Cu wire was connected to the front of the electrode with silver paint to provide an electrical connection, which was then enclosed in a glass tube. Epoxy (Loctite 9460 epoxy adhesive) was then used to cover the back, edges, and some of the front of the wafer to only leave a certain controlled electrochemically active surface area exposed to the electrolyte, which was measured to be between 0.3 and 0.6 cm^2 on each electrode. The epoxy was allowed to cure overnight at room temperature.

Electrochemical Setup and Testing. Round-bottom three-necked flasks (Sigma-Aldrich) were used for all tests with working electrodes prepared as described above, a Ag/AgCl reference electrode (CH Instruments), and a carbon cloth (Fuel Cell Store) counter electrode. A stir bar was used to continuously stir the electrolyte during all of the tests. The working electrodes were first cycled from 0.7 V to −0.7 V vs the Ag/AgCl reference electrode in 0.5 M H$_2$SO$_4$ (Sigma-Aldrich) to ensure that the curves appeared as shown in Figure 1a with no other peaks, following which they were rinsed with deionized water and dried with a nitrogen gun. Three different CuSO$_4$ concentrations (1 μM, 1 mM, and 50 mM) were used, prepared by dissolving CuSO$_4$ (Sigma-Aldrich) in 0.5 M H$_2$SO$_4$ as the electrolyte. For Pt, we also studied the 10 mM CuSO$_4$ concentration for electrochemical tests to observe the effects of a range of concentrations on HER. Cyclic voltammetry and chronoamperometry tests were performed on a Bio-Logic VMP3 potentiostat.

Scanning Electron Microscopy (SEM). SEM scans were collected using a Tescan Mira3 XM FEG-SEM instrument with a 5 kV operating voltage.

Atomic Force Microscopy (AFM). AFM was carried out on a Bruker Dimension Icon system, in noncontact or tapping mode.

X-ray Photoelectron Spectroscopy (XPS). XPS spectra were collected on a Nexsa G2 Surface Analysis System with a monochromated Al Kα X-ray source (source energy = 1486.6 eV). The flood gun was turned on while all scans were collected to minimize charging. For element scans, the pass energy was 50 eV, the step size was 0.1 eV, the dwell time was 50 ms, the X-ray spot size was 400 μm, and the number of sweeps was set to 3.

Elemental quantification was performed using Cu 2p$_{3/2}$, Pt 4f$_{7/2}$, and Au 4f peaks. Since the Pt 4f region overlaps with the Cu 3p region, peaks were deconvoluted using synthetic components for quantification of Cu deposited on Pt. In particular, a Doniach−Sunjic asymmetric line shape[68] was used for the Pt 4f peaks, while a pure Lorentzian peak shape was used for Cu 3p. Scofield relative sensitivity factors (RSFs)[69] were used in quantification together with the instrument-measured transmission function and effective attenuation length correction (EAL).[70] CasaXPS v2.3.6rev1.0Q was employed for all data processing tasks.[71] The inelastically scattered background was subtracted using Shirley's background.[72]

■ RESULTS AND DISCUSSION

To investigate electrochemical differences between Pt and Au electrodes in an acidic medium, cyclic voltammetry (CV) tests were conducted between −0.7 V and +0.7 V vs Ag/AgCl at a sweep rate of 20 mV/s. In Figure 1a, CV results are shown in an electrolyte of 0.5 M sulfuric acid, showing the difference between Pt and Au electrodes for catalyzing HER. As expected, Pt shows an earlier onset of the HER current (at about −0.27 V vs Ag/AgCl) than Au (−0.55 V vs Ag/AgCl), and the Pt electrode shows much higher current density.

Figure 1b shows CV curves with the same sulfuric acid electrolyte but now containing 50 mM CuSO$_4$. In both cases, there are obvious changes in the electrochemical response when Cu is present compared with the pure sulfuric acid electrolyte. When sweeping cathodically from an open circuit, there is a current density increase at ∼−0.27 V vs Ag/AgCl observed for Pt which can likely be ascribed to HER, which reaches a maximum value of ∼−13 mA cm^{-2}, after which it

stabilizes. The latter trend is likely due to Cu deposition interfering with HER at that point, causing the current density curve to flatten. As the Pt electrode is then swept to positive potentials starting from −0.7 V vs Ag/AgCl, some of the Cu that was reduced and deposited on the electrode is oxidized, as indicated by the large oxidation peak seen at ∼0.2 V vs Ag/AgCl. The shape of the CV curve for Au is similar to that for Pt, with the biggest difference being that there is very little HER for Au since the onset of HER on Au is ∼−0.55 V vs Ag/AgCl (Figure 1a), implying that all of the cathodic current is from Cu electrodeposition. The current density of the oxidation peak is also slightly smaller for Au compared to Pt and is offset to higher potentials.

Figure 1c,d shows CV curves for Pt (Figure 1c) and Au (Figure 1d) electrodes in sulfuric acid electrolyte with different concentrations of CuSO$_4$, varying from 1 μM to 50 mM. The CV curves for electrolytes without any CuSO$_4$ are plotted in dotted black lines, while those with varying amounts of CuSO$_4$ are plotted in solid, colored lines. The inset plots show magnified features at current densities near zero. For Pt (Figure 1c), the cathodic current generally decreases with an increasing Cu concentration. At 1 μM CuSO$_4$, the shape of the CV curve is nearly the same as that in pure sulfuric acid, where the majority of the cathodic current is due to HER. For 1 mM CuSO$_4$, the cathodic current density observed at −0.7 V vs Ag/AgCl decreases by about 10 mA cm^{-2}, which indicates that Cu deposition is taking place along with the HER, decreasing the overall current density. The current density is further decreased with 10 mM CuSO$_4$, pointing toward a competing effect between Cu deposition and HER in this potential range. 50 mM CuSO$_4$ also shows lower current density but has a different shape than the other CV curves, owing to limited HER and increased Cu deposition. The Cu oxidation peak is at 0.1−0.2 V vs Ag/AgCl and also significantly increases in magnitude with Cu concentration. For the Au electrodes (Figure 1d), there is a similar decreasing trend in current density from 1 μM to 1 mM CuSO$_4$ at very negative potentials. For 50 mM CuSO$_4$, however, the cathodic current density is higher, and the shape of the CV curve is also different, which is likely due to increased Cu deposition on Au.

Figure 1c and 1d also shows that the cathodic current density increase is at higher potentials with 50 mM CuSO$_4$ compared to lower concentrations. This trend is shown clearly by the linear sweep voltammetry (LSV) curves shown in Supporting Information (SI) Figure S1a-b. The greater Cu concentration causes greater current density at higher potentials. We also note that for the CV tests in Figure 1b−d the fifth CV cycle is displayed. Figure S1c,d shows the first CV cycle for electrodes in a sulfuric acid electrolyte containing 50 mM CuSO$_4$, along with the fifth cycle.

While CV experiments offer valuable comparative information, to qualitatively and quantitatively compare Cu deposition behavior, chronoamperometry was carried out to estimate the effect of Cu on the HER under different electrochemical conditions. This was done by holding Au and Pt electrodes at three different potentials: −0.1 V, −0.25 V, and −0.4 V vs Ag/AgCl, using LSV. At these potentials, it is expected to observe almost no HER, a minor amount of HER, and an increased HER, respectively. After LSV, chronoamperometry was carried out on each sample by holding it at a potential for either 20 s or 5 min, leading to a total of six different electrochemical test conditions. One such set of chronoamperometry curves is shown in Figure 2a, for Au electrodes held at −0.1 V vs Ag/
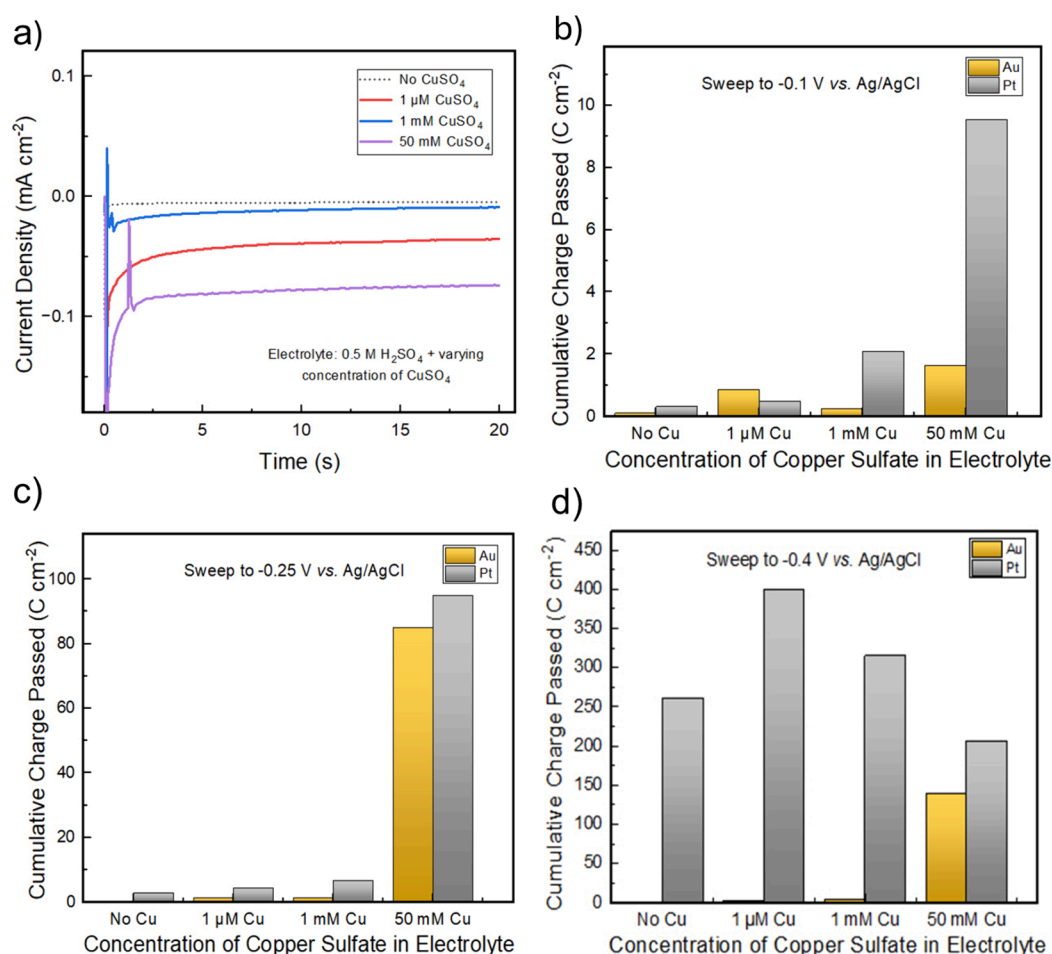
Figure 2. (a) Chronoamperometry tests for Au electrodes at -0.1 V vs Ag/AgCl for 20 s in 0.5 M H_2SO_4 (dotted black), 0.5 M H_2SO_4 + 1 μM $CuSO_4$ (red), 0.5 M H_2SO_4 + 1 mM $CuSO_4$ (blue), and 0.5 M H_2SO_4 + 50 mM $CuSO_4$ (purple). (b), (c), and (d) Chronoamperometry curves integrated over 20 s for Au and Pt electrodes in different Cu concentration electrolytes swept to -0.1 V, -0.25 V, and -0.4 V vs Ag/AgCl, respectively.

AgCl for 20 s. The remaining sets of chronoamperometry curves for Au electrodes are shown in Figures S2−S6, and the full sets of chronoamperometry curves for Pt electrodes are shown in Figures S7−S12. These plots are integrated with respect to time and plotted to obtain the total charge passed at each electrochemical condition for each Cu concentration. The resulting bar plots are shown in Figure 2b−d.

As shown in Figure 2b, the current density and hence charge that passed through the electrodes at -0.1 V vs Ag/AgCl was very low ($<$10 C cm^{-2}) since there is no HER and limited Cu deposition. There is a trend of increasing charge passed through Pt electrodes with increased $CuSO_4$ concentration, but there is no clear trend seen for Au electrodes. For the integrated charge passed at -0.25 V vs Ag/AgCl (Figure 2c), there is an increasing trend with concentration for both electrodes, with the total charge being higher by an order of magnitude for the 50 mM $CuSO_4$. In addition, there is more total charge passed at this more negative potential compared to that in Figure 2b.

There is a different trend for the Pt electrode at -0.4 V vs Ag/AgCl (Figure 2d). The total charge increases in electrolytes going from zero to 1 μM $CuSO_4$, before then decreasing as the $CuSO_4$ concentration continues to increase. This is consistent with the CV curves in Figure 1, where increasing $CuSO_4$ concentration decreased the cathodic current on Pt electrodes.

This suggests that Cu deposition interferes with HER and is likely limiting the activity of the catalyst material to evolve hydrogen. In contrast to this behavior, the Au electrodes in Figure 2d show similar behavior as at the lower potentials, where the total charge increases with $CuSO_4$ concentration. Thus, we see divergent electrochemical behavior from electrocatalytic vs nonelectrocatalytic electrodes.

Scanning electron microscopy (SEM) was used to image the surfaces of the electrodes after deposition under six different electrochemical conditions (1 and 50 mM $CuSO_4$ held at different potentials). The goal was to examine the morphology and extent of coverage of the deposited Cu on both Pt and Au electrodes. Figure 3a−c shows the surface of Au electrodes using 0.5 M H_2SO_4 + 1 mM $CuSO_4$ electrolyte, after being swept to -0.1 V, -0.25 V, and -0.4 V vs Ag/AgCl and holding for 5 min. The electrode surface is bare at -0.1 V vs Ag/AgCl (Figure 3a), implying that there is no deposition or that the deposition is too fine-grained to be observed with SEM, and while there are noticeable Cu deposits at -0.25 V vs Ag/AgCl (Figure 3b), a significant portion of the electrode surface is bare. It is more extensively covered at -0.4 V vs Ag/AgCl (Figure 3c). Figure 3d−f shows similar results but for Au electrodes in the higher-concentration 50 mM $CuSO_4$ electrolyte. After holding at -0.1 V vs Ag/AgCl for 5 min (Figure 3d), there is noticeable deposition of small-grained Cu.
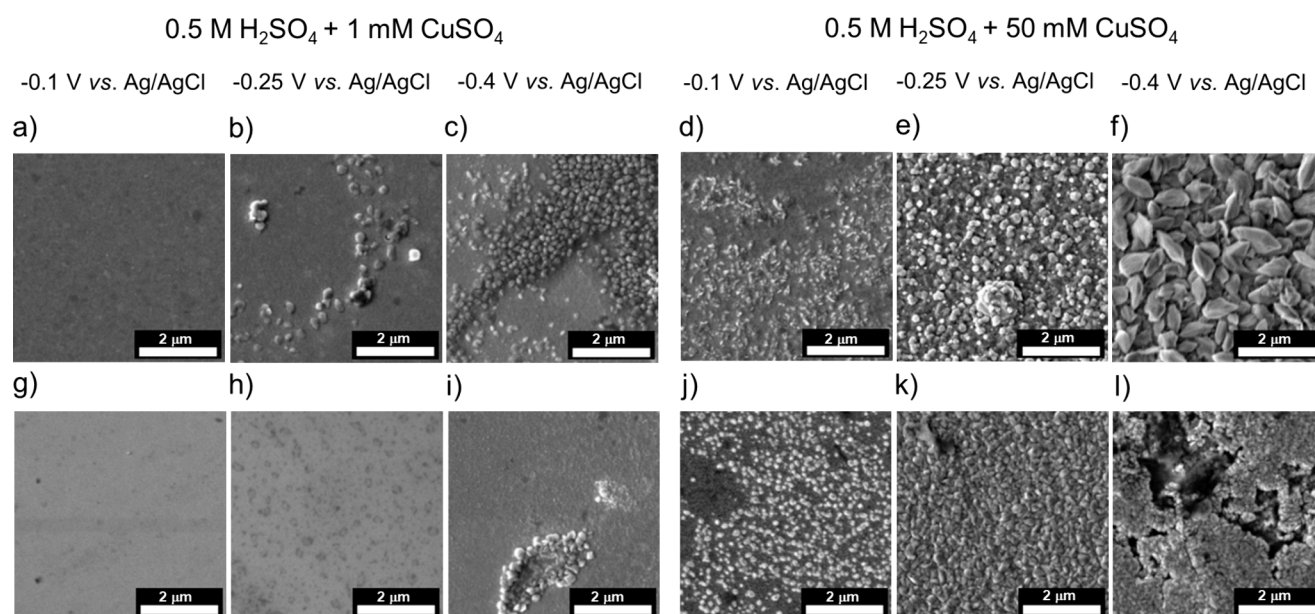
0.5 M H$_2$SO$_4$ + 1 mM CuSO$_4$ 0.5 M H$_2$SO$_4$ + 50 mM CuSO$_4$

-0.1 V vs. Ag/AgCl   -0.25 V vs. Ag/AgCl   -0.4 V vs. Ag/AgCl   -0.1 V vs. Ag/AgCl   -0.25 V vs. Ag/AgCl   -0.4 V vs. Ag/AgCl

Figure 3. (a−f) SEM images of Au electrodes in 0.5 M H$_2$SO$_4$ with 1 mM CuSO$_4$ electrolyte swept to (a) −0.1 V vs Ag/AgCl, (b) −0.25 V vs Ag/AgCl, and (c) −0.4 V vs Ag/AgCl and with 50 mM CuSO$_4$ in the electrolyte swept to (d) −0.1 V vs Ag/AgCl, (e) −0.25 V vs Ag/AgCl, and (f) −0.4 V vs Ag/AgCl. (g−l) SEM images of Pt electrodes in 0.5 M H$_2$SO$_4$ with 1 mM CuSO$_4$ electrolyte swept to (g) −0.1 V vs Ag/AgCl, (h) −0.25 V vs Ag/AgCl, and (i) −0.4 V vs Ag/AgCl and with 50 mM CuSO$_4$ in the electrolyte swept to (j) −0.1 V vs Ag/AgCl, (k) −0.25 V vs Ag/AgCl, and (l) −0.4 V vs Ag/AgCl.

At −0.25 V vs Ag/AgCl (Figure 3e), there is more significant deposition that covers the entire electrode surface, and there are also clusters of deposits observed at various locations. At −0.4 V vs Ag/AgCl, the Cu deposition covers the entire electrode (Figure 3f). The Cu grains are larger and are more angular and faceted than in the other cases, and there was also no noticeable variation of the thickness of the Cu deposits across the electrode surface.

Pt surfaces were also investigated for comparison to Au, as shown in Figure 3g−l. There is no obvious deposition at 1 mM CuSO$_4$ concentration at either −0.1 V or −0.25 V vs Ag/AgCl (Figure 3g,h, respectively). Although the electrode surface in Figure 3h appears more textured, SEM alone is not sufficient to detect potentially minimal Cu deposition. At −0.4 V vs Ag/AgCl, there are clusters of deposits observed on the surface of the Pt electrode (Figure 3i). For the 50 mM CuSO$_4$ concentration (Figure 3j−l), more of the electrode area is covered with deposition. At −0.1 V vs Ag/AgCl, there is significant deposition, but there are still bare spots left on the surface (Figure 3j). The surface is completely covered at −0.25 V vs Ag/AgCl (Figure 3k). At −0.4 V vs Ag/AgCl, there is significant deposition, and several areas on the electrode have discontinuities near the surface, leading to the formation of voids or craters (Figure 3l).

This direct comparison of electrode surfaces reveals some subtle differences in the way Cu is observed to grow on Pt and Au under various conditions. By comparing Figure 3b (Au) with Figure 3h (Pt) and also Figure 3c with Figure 3i, we notice that deposition is finer or has smaller grains on Pt than on Au, with the latter showing increased areal coverage under the same electrochemical conditions. However, the most important difference between Au and Pt is apparent by comparing the behavior at higher CuSO$_4$ concentrations and at more negative potentials (Figure 3f and l). With 50 mM CuSO$_4$, Cu deposition is the dominant reaction on Au, leading to large deposits uniformly covering the entire electrode

surface (Figure 3f). With the same concentration on Pt, there is also significant HER taking place at −0.4 V vs Ag/AgCl since Pt is electrocatalytic. It is likely that the tendency toward hydrogen evolution at this potential leads to the formation of the crater-like structures seen in Figure 3l that disrupt uniform Cu deposition, highlighting the stronger effect of these competing reactions on resulting Cu deposition morphology on an electrocatalytic material like Pt.

Atomic force microscopy (AFM) was used to investigate the topographic profiles of the electrodes after electrochemical treatment. Figure 4a and c shows SEM images, while Figure 4b and d shows AFM height maps from Au and Pt electrodes.
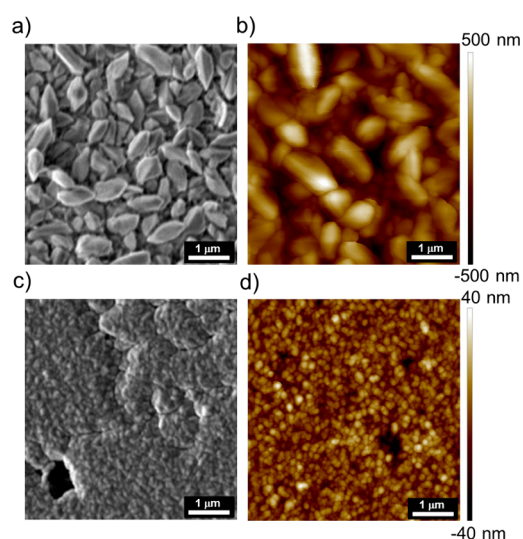

Figure 4. SEM images of (a) Au and (c) Pt electrodes and AFM height scans of (b) Au and (d) Pt electrodes swept to −0.4 V vs Ag/AgCl and held for 5 min in 0.5 M H$_2$SO$_4$ with 50 mM CuSO$_4$ (5 by 5 μm^2 scan area for all).
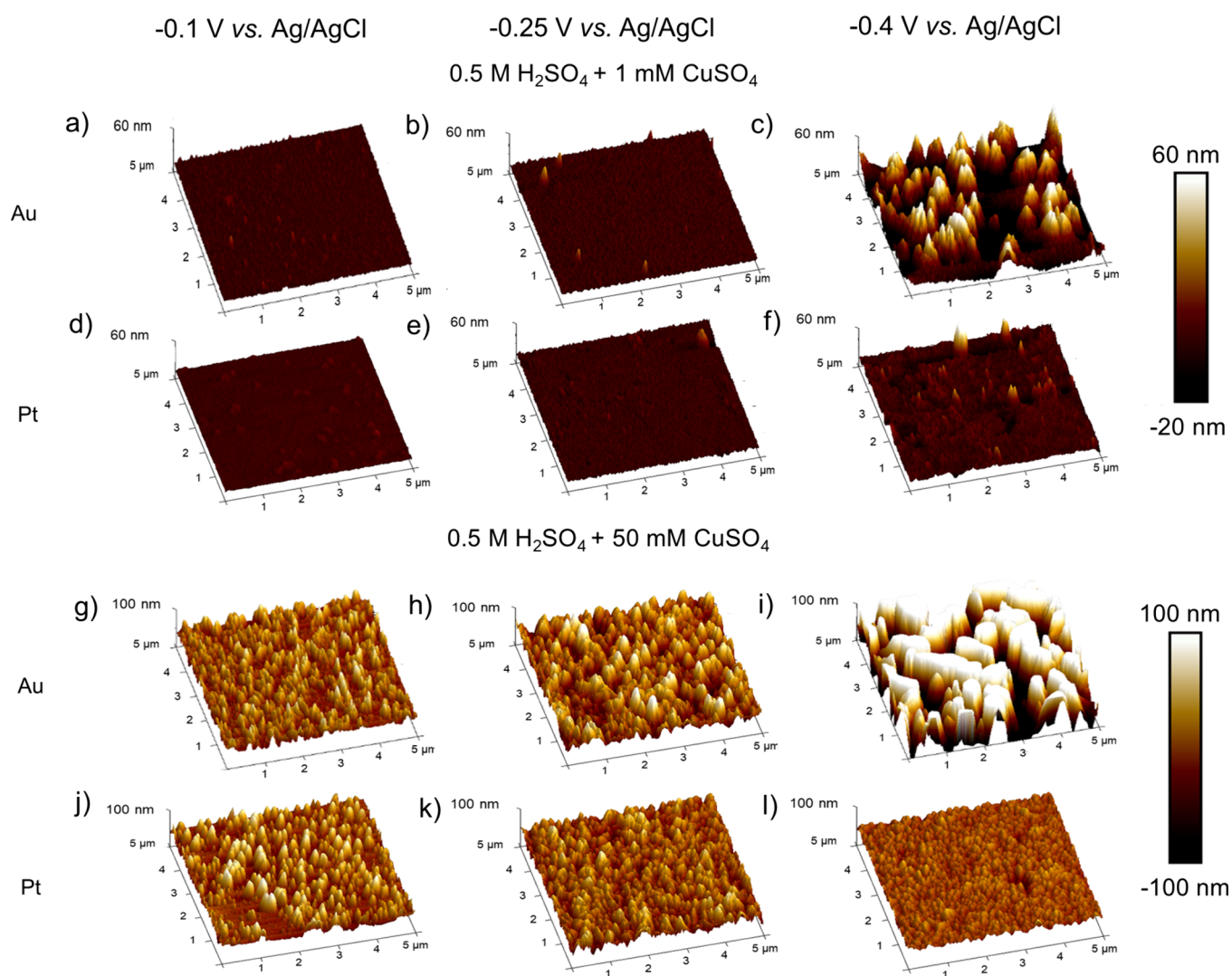
Figure 5. AFM 3D height scans of Au electrodes in 0.5 M H_2SO_4 with 1 mM $CuSO_4$ electrolyte swept to and held for 5 min at (a) −0.1 V vs Ag/AgCl, (b) −0.25 V vs Ag/AgCl, and (c) −0.4 V vs Ag/AgCl and of Pt electrodes in the same electrolyte swept to and held for 5 min at (d) −0.1 V vs Ag/AgCl, (e) −0.25 V vs Ag/AgCl, and (f) −0.4 V vs Ag/AgCl. AFM 3D height scans of Au electrodes in 0.5 M H_2SO_4 with 50 mM $CuSO_4$ electrolyte swept to and held for 5 min at (g) −0.1 V vs Ag/AgCl, (h) −0.25 V vs Ag/AgCl, and (i) −0.4 V vs Ag/AgCl and of Pt electrodes in the same electrolyte swept to and held for 5 min at (j) −0.1 V vs Ag/AgCl, (k) −0.25 V vs Ag/AgCl, and (l) −0.4 V vs Ag/AgCl.

Figure 4a and b depicts an SEM image and AFM tapping mode scan, respectively, of a Au electrode swept to −0.4 V vs Ag/AgCl and held for 5 min (50 mM $CuSO_4$ in the acidic electrolyte). The morphology of the deposits in the AFM scan correlates well with that of the SEM image. The AFM scan reveals irregularities in the height of the deposits, with height variations on the micron scale.

Figure 4c and d shows the SEM image and AFM scan of the surface of a Pt electrode after treatment under the same electrochemical conditions. The Cu grains and height variations are much smaller on the Pt electrode, with grain heights having only ∼30 nm of height variation across this 25 μm^2 scan. Furthermore, Figure 4c and d shows similar crater-like regions as observed previously, which may be due to hydrogen production and bubbling activity on the surface.

To further probe how sample topography is impacted by electrochemical conditions, we compared AFM height maps of Au and Pt electrodes tested at 1 mM $CuSO_4$ and 50 mM $CuSO_4$ concentrations held at different potentials for 5 min (Figure 5).

As shown in Figure 5a, with 1 mM $CuSO_4$, there is insignificant height variation at −0.1 V vs Ag/AgCl on Au, which agrees with the SEM image (Figure 3a). At −0.25 V vs Ag/AgCl (Figure 5b), there are a few deposits on the surface, each a few nanometers in height. At −0.4 V vs Ag/AgCl (Figure 5c), the deposits are taller (>60 nm) and cover more electrode surface area. Figure 5d−f shows similar experiments with a Pt electrode. Figure 5d and e (−0.1 and −0.25 V vs Ag/AgCl) shows mostly bare surfaces. At −0.4 V vs Ag/AgCl (Figure 5f), there is a greater number of deposits, but there is less deposition than on the Au electrode in Figure 5c. This is consistent with the deposition being more fine-grained on Pt than on Au for this 1 mM $CuSO_4$ concentration.

Figure 5g−l shows AFM scans of Au and Pt with a higher concentration of $CuSO_4$ in the electrolyte (50 mM). Figure 5g shows significant deposition over the entire area of the electrode surface in the scan, even at −0.1 V vs Ag/AgCl on Au, with the deposits growing slightly larger for the −0.25 V vs Ag/AgCl case (Figure 5h). At −0.4 V vs Ag/AgCl (Figure 5i), the deposits become up to ∼1 μm in size (as discussed in
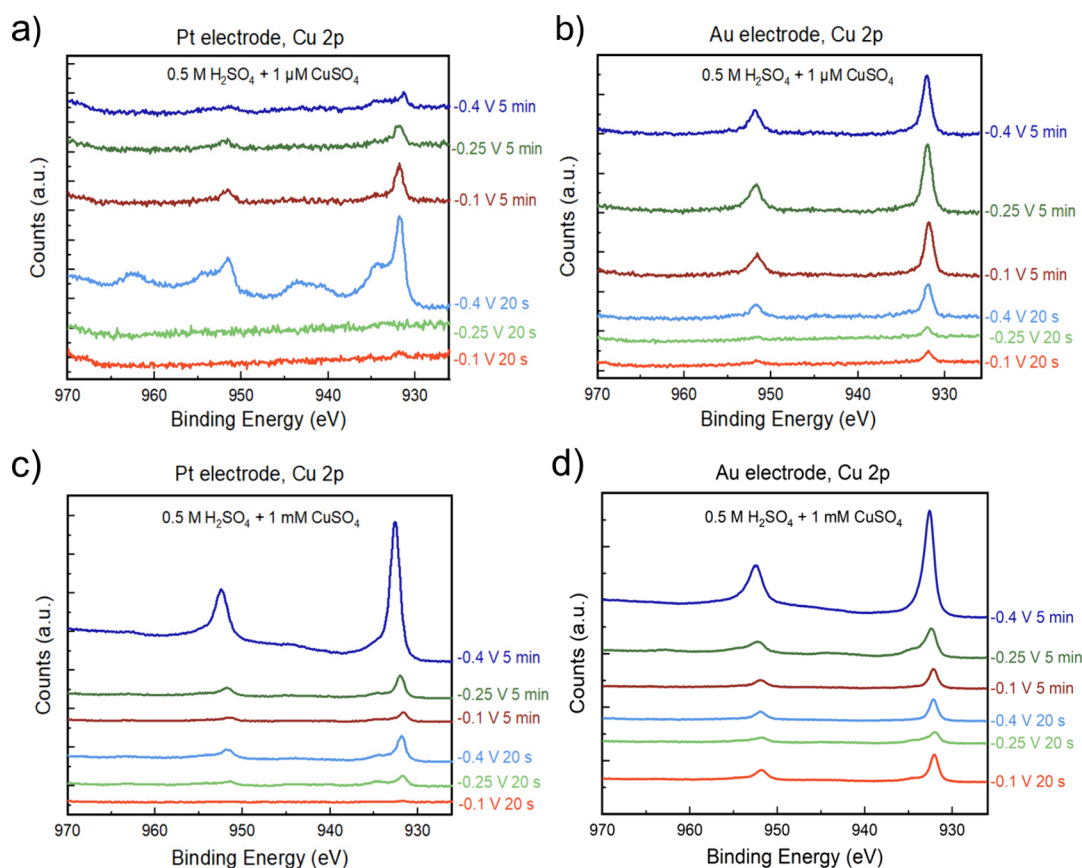
Figure 6. XPS scans of Cu 2p spectra for (a) Pt electrodes in 0.5 M H_2SO_4 with 1 μM $CuSO_4$ electrolyte, (b) Au electrodes in 0.5 M H_2SO_4 with 1 μM $CuSO_4$, (c) Pt electrodes in 0.5 M H_2SO_4 with 1 mM $CuSO_4$ electrolyte, and (d) Au electrodes in 0.5 M H_2SO_4 with 1 mM $CuSO_4$. Samples were swept to −0.1 V vs Ag/AgCl for 20 s and 5 min (light red and dark red), −0.25 V vs Ag/AgCl for 20 s and 5 min (light green and dark green), and −0.4 V vs Ag/AgCl for 20 s and 5 min (light blue and dark blue).

Figure 4b). While there is also significant deposition observed at −0.1 V vs Ag/AgCl on Pt in Figure 5j, there are still some bare spots left on the surface. There are no noticeable bare spots at −0.25 V vs Ag/AgCl (Figure 5k); however, the height of the deposits is more consistent than that at −0.1 V vs Ag/AgCl. This trend of decreasing variation in the height of the deposit at more negative potentials on Pt continues at −0.4 V vs Ag/AgCl, where in Figure 5l the surface is flatter and more uniform than in the previous two cases. This is the opposite trend to the Au case.

While SEM and AFM are useful for providing insight into the growth and morphology of Cu on Pt and Au under the electrochemical conditions tested, these techniques do not provide adequate insight into whether deposition takes place at the lower concentration of 1 μM $CuSO_4$, where the grain size of Cu may be too small to be observed. Since this is a relevant concentration to understand the effect of impurity ions in seawater interfering with HER, we use X-ray photoelectron spectroscopy (XPS) to probe this case. As a surface-sensitive technique, we expect to detect trace amounts of Cu deposition on the two substrates in the 0.5 M H_2SO_4 + 1 μM $CuSO_4$ electrolyte, depending on the electrochemical conditions used.

Figure 6 shows the Cu 2p spectra for the 1 μM and 1 mM $CuSO_4$ cases on Pt and Au electrodes for all six electrochemical tests. Spectra were collected from at least two points on each sample to ensure the uniformity of coverage. Figure 6a shows the Cu 2p scans from electrochemical testing at various potentials and times on Pt electrodes in a 1 μM $CuSO_4$

electrolyte. For electrodes held at −0.1 V and −0.25 V vs Ag/AgCl for only 20 s, there are no Cu 2p peaks, indicating that Cu deposition had not taken place. For the electrode held at −0.4 V vs Ag/AgCl for 20 s, there are characteristic Cu $2p_{3/2}$ (932.6 eV) and Cu $2p_{1/2}$ peaks observed, indicating Cu deposition, likely in the form of CuO as indicated by the presence of weak satellite peaks.[73] For electrodes held at all three potentials for 5 min, the Cu 2p doublet is also visible. These results imply that Cu deposition takes place in parallel with the HER on Pt electrodes even at the very dilute concentrations found in seawater. On Au electrodes in the same dilute electrolyte (1 μM $CuSO_4$), Cu deposition is observed in all six cases (Figure 6b). Thus, Cu deposition occurs more readily on Au than on Pt, possibly because of the competition with the HER on Pt.

For the electrolyte containing 1 mM $CuSO_4$, peaks are observed for all electrochemical conditions on a Pt electrode (Figure 6c), indicating a greater deposition of Cu or Cu oxides on the electrode surface with this increased $CuSO_4$ concentration. The magnitude of the peaks enlarges as the potential is held at more negative values for a given time. For the same electrolyte concentration tested on Au electrodes, the spectra shown in Figure 6d similarly indicate deposition occurring in all cases, as Cu metal or Cu oxides. XPS data for samples tested in electrolytes containing 50 mM $CuSO_4$ are shown in SI Figure S13.

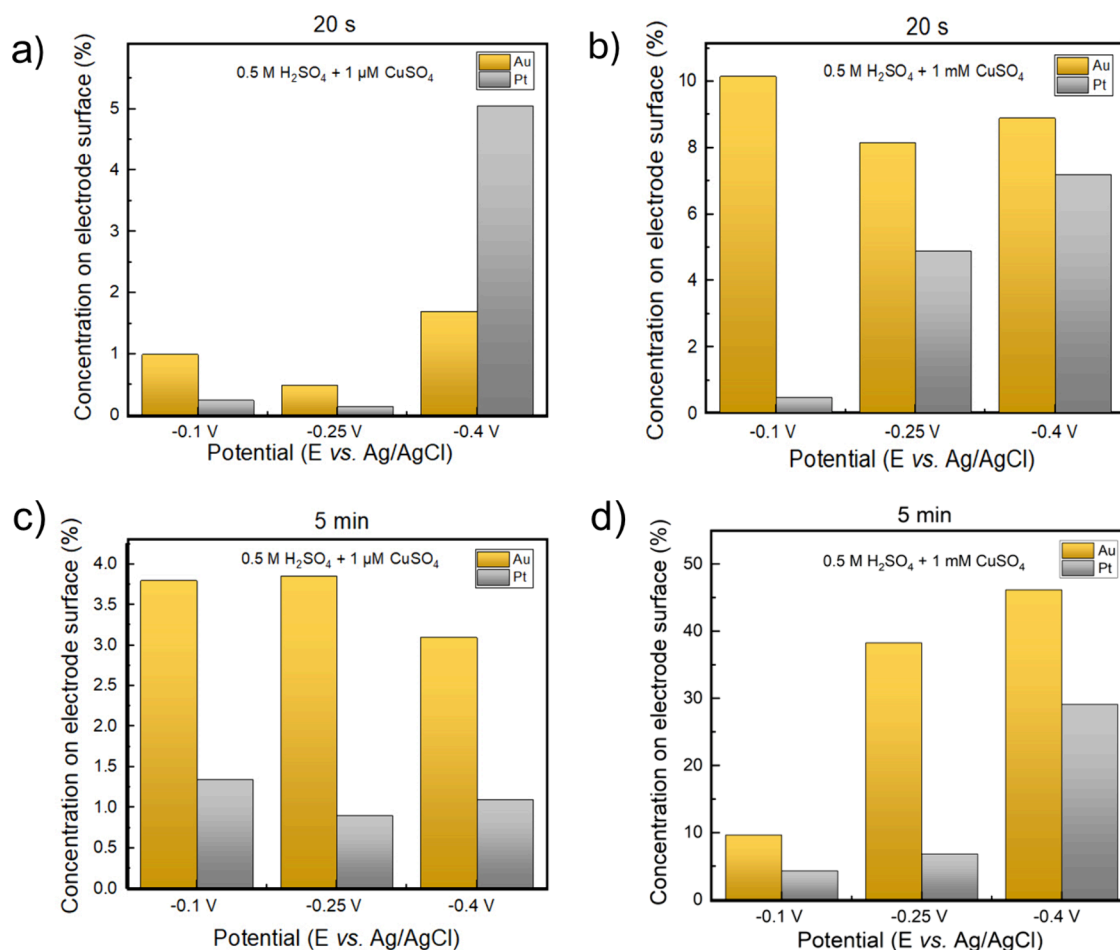We also collected the Pt 4f and Au 4f XPS spectra for all samples, as shown in SI Figure S14. At 50 mM $CuSO_4$, there

Figure 7. Calculated percentages of Cu on Au and Pt electrode surfaces from XPS data for samples in 0.5 M H$_2$SO$_4$ with 1 μM CuSO$_4$ swept to different potentials and held for (a) 20 s and (c) 5 min and for samples in 0.5 M H$_2$SO$_4$ with 1 mM CuSO$_4$ held for (b) 20 s and (d) 5 min.

are no Au peaks detected from the Au electrodes apart from the samples swept to −0.1 V vs Ag/AgCl, indicating that the Cu completely covered the surface of the electrode (thicker than at least a few nanometers) in all other cases, leaving no Au exposed. For Pt electrodes, the Pt 4f doublet also diminishes with Cu deposition at lower potentials and longer times. A new set of peaks arises around 75−80 eV binding energy, which is ascribed to Cu 3p. As more Cu is deposited, the Cu 3p peak intensity increases until it dominates the Pt 4f signal since it is in a similar binding energy range.

Apart from a qualitative analysis, we also conducted a quantitative analysis of the XPS data to find the quantity of Cu on Au and Pt electrode surfaces after treatment under different electrochemical conditions. Cu 2p$_{3/2}$, Pt 4f$_{7/2}$, and Au 4f peaks were utilized in quantitative analysis and to account for the differences in kinetic energies of the peaks used in quantification. Effective attenuation length (as described by Seah) was utilized.[70] The quantification results are shown as bar plots in Figure 7. Figure 7a shows the quantitative analysis for Au and Pt electrodes in a 0.5 M H$_2$SO$_4$ + 1 μM CuSO$_4$ electrolyte, with the electrodes held at 0.1 V, −0.25 V, and −0.4 V vs Ag/AgCl for 20 s. The extent of Cu surface coverage is less than 2% for Au and less than 5% for Pt. While this is a low total percentage, this still means that a portion of the electrode surface is poisoned by Cu deposition even at this very dilute concentration over limited time. For 1 mM CuSO$_4$ after 20 s (Figure 7b), more Cu is present. On Au, a relatively

higher concentration of Cu is present (8−10%). While the percentage is lower for Pt compared to Au at all potentials, it is still seen to increase as observed in Figure 7a, particularly for −0.25 V and −0.4 V vs Ag/AgCl.

To observe the trends over a longer deposition period, this quantitative analysis was performed on samples held at these potentials for 5 min. Figure 7c shows the comparison for the electrodes in a 0.5 M H$_2$SO$_4$ + 1 μM CuSO$_4$ electrolyte. There is an increase in areal coverage for all cases compared to Figure 7a when holding at a potential for a longer duration at the same concentration, except for Pt at −0.4 V vs Ag/AgCl. This could be due to HER starting to dominate over time in the presence of very limited Cu present in the electrolyte, or it could simply be due to variability in the XPS data. Similarly, for samples held for 5 min in the electrolyte containing 1 mM CuSO$_4$ (Figure 7d), the concentration of Cu on Au electrodes increased 5 times for samples swept to −0.25 V and −0.4 V vs Ag/AgCl, while it appears to be consistent for −0.1 V vs Ag/AgCl. There is an increase in the extent of deposition observed for Pt electrodes as well, compared with Figure 7b. Both Figure 7c and d for samples held at 5 min show more deposition on Au electrodes compared with Pt. Additionally, for cases involving higher concentrations of CuSO$_4$ in the electrolyte, as well as more negative potentials and longer deposition times, there was generally an increased concentration of sulfur detected on the surface, possibly owing to the greater content of sulfate ions present in the electrolyte.

CONCLUSIONS

Impurities are a major concern for electrolyzers using direct seawater splitting. This study shows that Cu ions in solution can significantly affect the HER on catalytic surfaces. Increased $CuSO_4$ concentration caused more substantial electrodeposition, indicating that impurity buildup over extended electrolyzer operation can have a substantial effect and poison a catalyst. Cyclic voltammetry tests showed a decrease of the current density with increasing $CuSO_4$ concentration for both Pt and Au electrodes, which points to a poisoning effect. Integrated charge plots obtained from chronoamperometry curves indicated a similar decrease in total charge passed as the concentration of $CuSO_4$ was increased from 1 μM to 50 mM for Pt for the −0.4 V vs Ag/AgCl case. However, a similar clear trend was not seen for Au, which is likely because the HER does not compete with Cu deposition to the same extent on Au, owing to its lower electrocatalytic activity for HER.

Surface analysis of the electrodes via SEM and AFM suggested that Cu deposits have different morphologies and larger sizes on Au than on Pt. At high $CuSO_4$ concentration and low potentials, Pt electrodes showed signs of the deposited Cu being damaged, which is potentially due to hydrogen evolution and bubbling. This is in contrast to the regular and uniform deposition observed on Au. This was confirmed by testing several samples, ensuring the reliability and repeatability of the deposition trends on both electrodes. XPS confirmed the presence of Cu even at the lowest considered concentration of 1 μM $CuSO_4$. Thus, the electrocatalytic activity of the electrode material appears to affect the nature and morphology of metal deposition when the HER and metal electrodeposition are occurring simultaneously.

These trends showcase a competition between HER and Cu electrodeposition, revealed by using surface analysis techniques at higher Cu concentrations. However, Cu deposition was observed even at low concentrations (similar to its concentration in seawater), indicating a likelihood of competing effects that are essential to consider in the design of appropriate catalysts, especially ones that can maintain optimum operating efficiency over extended use.

These findings highlight the importance of studying mechanisms associated with impurities to determine their effects on fuel-producing reactions, with further work needed to simulate the complex real case of seawater where multiple types of ions are present. Additionally, *in situ* studies to provide greater insight into complex electrochemical behavior and the competing electrochemical reactions in the presence of impurities would be beneficial. *In situ* studies could also prove useful in identifying the mechanism of nucleation and growth of impurities on different substrates in the early stages and whether this is dependent on the nature of the impurity itself and/or the nature of the electrocatalyst. Finally, it is also of interest to study other impurities and different electrocatalysts, which may be engineered to avoid or limit poisoning.

ASSOCIATED CONTENT

ⓢ Supporting Information

The Supporting Information is available free of charge at https://pubs.acs.org/doi/10.1021/acsaem.4c02697.

Additional electrochemical data including cyclic voltammetry and chronoamperometry curves, XPS plots for Cu 2p in 0.5 M H_2SO_4 + 50 mM $CuSO_4$ electrolyte, and XPS spectra for Au 4f and Pt 4f in electrolytes with the various $CuSO_4$ concentrations (PDF)

AUTHOR INFORMATION

Corresponding Author

Matthew T. McDowell − *School of Materials Science & Engineering and George W. Woodruff School of Mechanical Engineering, Georgia Institute of Technology, Atlanta, Georgia 30332, United States;* ⓘ orcid.org/0000-0001-5552-3456; Email: mattmcdowell@gatech.edu

Authors

Sonakshi Saini − *School of Materials Science & Engineering, Georgia Institute of Technology, Atlanta, Georgia 30332, United States*

Salem C. Wright − *School of Materials Science & Engineering, Georgia Institute of Technology, Atlanta, Georgia 30332, United States*

Sahanaz Parvin − *Department of Chemical & Biomolecular Engineering, Lehigh University, Bethlehem, Pennsylvania 18015, United States*

Jonas Baltrusaitis − *Department of Chemical & Biomolecular Engineering, Lehigh University, Bethlehem, Pennsylvania 18015, United States;* ⓘ orcid.org/0000-0001-5634-955X

Complete contact information is available at:
https://pubs.acs.org/10.1021/acsaem.4c02697

Author Contributions

S.S.: Methodology, Investigation, Formal analysis, Validation, Writing - Original Draft, Writing - Review & Editing, and Visualization. S.C.W.: Investigation, Writing - Review & Editing. S.P.: Formal analysis. J.B.: Formal analysis, Writing - Review & Editing, Funding acquisition. M.T.M.: Conceptualization, Resources, Formal analysis, Validation, Writing - Review & Editing, Supervision, Funding acquisition, and Project administration.

Notes

The authors declare no competing financial interest.

REFERENCES

(1) Abdin, Z.; Zafaranloo, A.; Rafiee, A.; Mérida, W.; Lipiński, W.; Khalilpour, K. R. Hydrogen as an Energy Vector. *Renew. Sustain. Energy Rev.* **2020**, *120*, No. 109620.

(2) Falcone, P. M.; Hiete, M.; Sapio, A. Hydrogen Economy and Sustainable Development Goals: Review and Policy Insights. *Curr. Opinion Green Sustain. Chem.* **2021**, *31*, No. 100506.

(3) Hassan, Q.; Algburi, S.; Sameen, A. Z.; Salman, H. M.; Jaszczur, M. Green Hydrogen: A Pathway to a Sustainable Energy Future. *Int. J. Hydrogen Energy* **2024**, *50*, 310−333.

(4) Hassan, Q.; Sameen, A. Z.; Olapade, O.; Alghoul, M.; Salman, H. M.; Jaszczur, M. Hydrogen Fuel as an Important Element of the

Energy Storage Needs for Future Smart Cities. *Int. J. Hydrogen Energy* **2023**, *48* (78), 30247−30262.

(5) He, W.; Abbas, Q.; Alharthi, M.; Mohsin, M.; Hanif, I.; Vinh Vo, X.; Taghizadeh-Hesary, F. Integration of Renewable Hydrogen in Light-Duty Vehicle: Nexus Between Energy Security and Low Carbon Emission Resources. *Int. J. Hydrogen Energy* **2020**, *45* (51), 27958−27968.

(6) Yang, M.; Hunger, R.; Berrettoni, S.; Sprecher, B.; Wang, B. A Review of Hydrogen Storage and Transport Technologies. *Clean Energy* **2023**, *7* (1), 190−216.

(7) Burton, N. A.; Padilla, R. V.; Rose, A.; Habibullah, H. Increasing the Efficiency of Hydrogen Production from Solar Powered Water Electrolysis. *Renew. Sustain. Energy Rev.* **2021**, *135*, No. 110255.

(8) Gahleitner, G. Hydrogen from Renewable Electricity: An International Review of Power-to-Gas Pilot Plants for Stationary Applications. *Int. J. Hydrogen Energy* **2013**, *38* (5), 2039−2061.

(9) Nasser, M.; Megahed, T. F.; Ookawara, S.; Hassan, H. A Review of Water Electrolysis-Based Systems for Hydrogen Production using Hybrid/Solar/Wind Energy Systems. *Environ. Sci. Pollut. Res.* **2022**, *29* (58), 86994−87018.

(10) Kumar, S. S.; Lim, H. An Overview of Water Electrolysis Technologies for Green Hydrogen Production. *Energy Rep.* **2022**, *8*, 13793−13813.

(11) Franco, A.; Giovannini, C. Recent and Future Advances in Water Electrolysis for Green Hydrogen Generation: Critical Analysis and Perspectives. *Sustainability* **2023**, *15* (24), 16917.

(12) Martínez de León, C.; Ríos, C.; Brey, J. J. Cost of Green Hydrogen: Limitations of Production from a Stand-Alone Photovoltaic System. *Int. J. Hydrogen Energy* **2023**, *48* (32), 11885−11898.

(13) Ramadan, M. M.; Wang, Y.; Tooteja, P. Analysis of Hydrogen Production Costs Across the United States and Over the Next 30 Years. *arXiv:2206.10689*, **2022**.

(14) Farràs, P.; Strasser, P.; Cowan, A. J. Water Electrolysis: Direct from the Sea or Not to Be? *Joule* **2021**, *5* (8), 1921−1923.

(15) Veroneau, S. S.; Nocera, D. G. Continuous Electrochemical Water Splitting from Natural Water Sources via Forward Osmosis. *Proc. Natl. Acad. Sci. U S A* **2021**, *118* (9), No. e2024855118.

(16) Guo, J.; Zheng, Y.; Hu, Z.; Zheng, C.; Mao, J.; Du, K.; Jaroniec, M.; Qiao, S.-Z.; Ling, T. Direct Seawater Electrolysis by Adjusting the Local Reaction Environment of a Catalyst. *Nat. Energy* **2023**, *8*, 264−272.

(17) Jiang, S.; Suo, H.; Zhang, T.; Liao, C.; Wang, Y.; Zhao, Q.; Lai, W. Recent Advances in Seawater Electrolysis. *Catalysts* **2022**, *12* (2), 123.

(18) Tong, W.; Forster, M.; Dionigi, F.; Dresp, S.; Sadeghi Erami, R.; Strasser, P.; Cowan, A. J.; Farras, P. Electrolysis of Low-Grade and Saline Surface Water. *Nat. Energy* **2020**, *5* (5), 367−377.

(19) Jin, H.; Xu, J.; Liu, H.; Shen, H.; Yu, H.; Jaroniec, M.; Zheng, Y.; Qiao, S.-Z. Emerging Materials and Technologies for Electrocatalytic Seawater Splitting. *Sci. Adv.* **2023**, *9* (42), No. eadi7755.

(20) Dresp, S.; Dionigi, F.; Klingenhof, M.; Strasser, P. Direct Electrolytic Splitting of Seawater: Opportunities and Challenges. *ACS Energy Lett.* **2019**, *4* (4), 933−942.

(21) Balaji, R.; Kannan, B. S.; Lakshmi, J.; Senthil, N.; Vasudevan, S.; Sozhan, G.; Shukla, A. K.; Ravichandran, S. An Alternative Approach to Selective Sea Water Oxidation for Hydrogen Production. *Electrochem. Commun.* **2009**, *11* (8), 1700−1702.

(22) Lindquist, G. A.; Xu, Q.; Oener, S. Z.; Boettcher, S. W. Membrane Electrolyzers for Impure-Water Splitting. *Joule* **2020**, *4* (12), 2549−2561.

(23) Xie, H.; Zhao, Z.; Liu, T.; Wu, Y.; Lan, C.; Jiang, W.; Zhu, L.; Wang, Y.; Yang, D.; Shao, Z. A Membrane-Based Seawater Electrolyser for Hydrogen Generation. *Nature* **2022**, *612*, 673−678.

(24) Dionigi, F.; Reier, T.; Pawolek, Z.; Gliech, M.; Strasser, P. Design Criteria, Operating Conditions, and Nickel-Iron Hydroxide Catalyst Materials for Selective Seawater Electrolysis. *ChemSusChem* **2016**, *9* (9), 962−972.

(25) Kuang, Y.; Kenney, M. J.; Meng, Y.; Hung, W. H.; Liu, Y.; Huang, J. E.; Prasanna, R.; Li, P.; Li, Y.; Wang, L.; Lin, M. C.;

McGehee, M. D.; Sun, X.; Dai, H. Solar-Driven, Highly Sustained Splitting of Seawater into Hydrogen and Oxygen Fuels. *Proc. Natl. Acad. Sci. U S A* **2019**, *116* (14), 6624−6629.

(26) Liu, G.; Xu, Y.; Yang, T.; Jiang, L. Recent Advances in Electrocatalysts for Seawater Splitting. *Nano Mater. Sci.* **2023**, *5* (1), 101−116.

(27) Liu, J.; Duan, S.; Shi, H.; Wang, T.; Yang, X.; Huang, Y.; Wu, G.; Li, Q. Rationally Designing Efficient Electrocatalysts for Direct Seawater Splitting: Challenges, Achievements, and Promises. *Angew. Chem., Int. Ed.* **2022**, *61* (45), No. e202210753.

(28) Yu, L.; Zhu, Q.; Song, S.; McElhenny, B.; Wang, D.; Wu, C.; Qin, Z.; Bao, J.; Yu, Y.; Chen, S.; Ren, Z. Non-Noble Metal-Nitride Based Electrocatalysts for High-Performance Alkaline Seawater Electrolysis. *Nat. Commun.* **2019**, *10* (1), 5106.

(29) Zheng, J. Seawater Splitting for High-Efficiency Hydrogen Evolution by Alloyed PtNi$_x$ Electrocatalysts. *Appl. Surf. Sci.* **2017**, *413*, 360−365.

(30) Zhuang, L.; Li, S.; Li, J.; Wang, K.; Guan, Z.; Liang, C.; Xu, Z. Recent Advances on Hydrogen Evolution and Oxygen Evolution Catalysts for Direct Seawater Splitting. *Coatings* **2022**, *12* (5), 659.

(31) Dresp, S.; Dionigi, F.; Loos, S.; Ferreira de Araujo, J.; Spori, C.; Gliech, M.; Dau, H.; Strasser, P. Direct Electrolytic Splitting of Seawater: Activity, Selectivity, Degradation, and Recovery Studied from the Molecular Catalyst Structure to the Electrolyzer Cell Level. *Adv. Energy Mater.* **2018**, *8*, No. 1800338.

(32) Becker, H.; Murawski, J.; Shinde, D. V.; Stephens, I. E. L.; Hinds, G.; Smith, G. Impact of Impurities on Water Electrolysis: A Review. *Sustain. Energy Fuels* **2023**, *7* (7), 1565−1603.

(33) Pan, Q.; Zhao, P.; Gao, L.; Liu, H.; Hu, H.; Dong, L. In-Depth Study on the Effects of Impurity Ions in Saline Wastewater Electrolysis. *Molecules* **2023**, *28* (12), 4576.

(34) Collier, A.; Wang, H.; Ziyuan, X.; Zhang, J.; Wilkinson, D. Degradation of Polymer Electrolyte Membranes. *Int. J. Hydrogen Energy* **2006**, *31* (13), 1838−1854.

(35) Hongsirikarn, K.; Goodwin, J. G., Jr; Greenway, S.; Creager, S. Effect of Cations (Na$^+$, Ca^{2+}, Fe^{3+}) on the Conductivity of a Nafion Membrane. *J. Power Sources* **2010**, *195* (21), 7213−7220.

(36) Kienitz, B. L.; Baskaran, H.; Zawodzinski, T. A., Jr Modeling the Steady-State Effects of Cationic Contamination on Polymer Electrolyte Membranes. *Electrochim. Acta* **2009**, *54* (6), 1671−1679.

(37) Schalenbach, M.; Keller, L.; Janotta, B.; Bauer, A.; Tempel, H.; Kungl, H.; Bonnet, M.; Eichel, R.-A. The Effect of Ion Exchange Poisoning on the Ion Transport and Conduction in Polymer Electrolyte Membranes (PEMs) for Water Electrolysis. *J. Electrochem. Soc.* **2022**, *169* (9), No. 094510.

(38) Zlobinski, M.; Babic, U.; Fikry, M.; Gubler, L.; Schmidt, T. J.; Boillat, P. Dynamic Neutron Imaging and Modeling of Cationic Impurities in Polymer Electrolyte Water Electrolyzer. *J. Electrochem. Soc.* **2020**, *167* (14), No. 144509.

(39) Uddin, M. A.; Qi, J.; Wang, X.; Pasaogullari, U.; Bonville, L. Distributed Cation Contamination from Cathode to Anode Direction in Polymer Electrolyte Fuel Cells. *Int. J. Hydrogen Energy* **2015**, *40* (38), 13099−13105.

(40) Banas, C. J.; Uddin, M. A.; Park, J.; Bonville, L. J.; Pasaogullari, U. Thinning of Cathode Catalyst Layer in Polymer Electrolyte Fuel Cells due to Foreign Cation Contamination. *J. Electrochem. Soc.* **2018**, *165* (6), F3015−F3023.

(41) Monteiro, M. C. O.; Goyal, A.; Moerland, P.; Koper, M. T. M. Understanding Cation Trends for Hydrogen Evolution on Platinum and Gold Electrodes in Alkaline Media. *ACS Catal.* **2021**, *11* (23), 14328−14335.

(42) Rakousky, C.; Reimer, U.; Wippermann, K.; Carmo, M.; Lueke, W.; Stolten, D. An Analysis of Degradation Phenomena in Polymer Electrolyte Membrane Water Electrolysis. *J. Power Sources* **2016**, *326*, 120−128.

(43) Strmcnik, D.; van der Vliet, D. F.; Chang, K. C.; Komanicky, V.; Kodama, K.; You, H.; Stamenkovic, V. R.; Marković, N. M. Effects of Li$^+$, K$^+$, and Ba^{2+} Cations on the ORR at Model and High Surface

Area Pt and Au Surfaces in Alkaline Solutions. *J. Phys. Chem. Lett.* **2011**, *2* (21), 2733−2736.

(44) Xue, S.; Garlyyev, B.; Watzele, S.; Liang, Y.; Fichtner, J.; Pohl, M. D.; Bandarenka, A. S. Influence of Alkali Metal Cations on the Hydrogen Evolution Reaction Activity of Pt, Ir, Au, and Ag Electrodes in Alkaline Electrolytes. *ChemElectroChem.* **2018**, *5* (17), 2326−2329.

(45) Nidola, A.; Schira, R. Poisoning Mechanisms and Structural Analyses on Metallic Contaminated Cathode Catalysts in Chlor-Alkali Membrane Cell Technology. *J. Electrochem. Soc.* **1986**, *133*, 1653−1656.

(46) Argyle, M.; Bartholomew, C. Heterogeneous Catalyst Deactivation and Regeneration: A Review. *Catalysts* **2015**, *5* (1), 145−269.

(47) Cimino, S.; Lisi, L. Catalyst Deactivation, Poisoning and Regeneration. *Catalysts* **2019**, *9* (8), 668.

(48) Vos, J. G.; Koper, M. T. M. Measurement of Competition Between Oxygen Evolution and Chlorine Evolution using Rotating Ring-Disk Electrode Voltammetry. *J. Electroanal. Chem.* **2018**, *819*, 260−268.

(49) Schmidt, T. J.; Paulus, U. A.; Gasteiger, H. A.; Behm, R. J. The Oxygen Reduction Reaction on a Pt/Carbon Fuel Cell Catalyst in the Presence of Chloride Anions. *J. Electroanal. Chem.* **2001**, *508*, 41−47.

(50) Markovic, N. M.; Gasteiger, H. A.; Grgur, B. N.; Ross, P. N. Oxygen Reduction Reaction on Pt(111): Effects of Bromide. *J. Electroanal. Chem.* **1999**, *467*, 157−163.

(51) Briega-Martos, V.; Mello, G. A. B.; Aran-Ais, R. M.; Climent, V.; Herrero, E.; Feliu, J. M. Understandings on the Inhibition of Oxygen Reduction Reaction by Bromide Adsorption on Pt(111) Electrodes at Different pH Values. *J. Electrochem. Soc.* **2018**, *165* (15), J3045−J3051.

(52) Lyu, X.; Serov, A. Cutting-Edge Methods for Amplifying the Oxygen Evolution Reaction During Seawater Electrolysis: A Brief Synopsis. *Ind. Chem. Mater.* **2023**, *1*, 475−485.

(53) Vos, J. G.; Venugopal, A.; Smith, W. A.; Koper, M. T. M. Competition and Selectivity During Parallel Evolution of Bromine, Chlorine and Oxygen on IrO$_x$ Electrodes. *J. Catal.* **2020**, *389*, 99−110.

(54) Cheng, N.; Stambula, S.; Wang, D.; Banis, M. N.; Liu, J.; Riese, A.; Xiao, B.; Li, R.; Sham, T. K.; Liu, L. M.; Botton, G. A.; et al. Platinum Single-Atom and Cluster Catalysis of the Hydrogen Evolution Reaction. *Nat. Commun.* **2016**, *7*, 13638.

(55) Hansen, J. N.; Prats, H.; Toudahl, K. K.; Morch Secher, N.; Chan, K.; Kibsgaard, J.; Chorkendorff, I. Is There Anything Better than Pt for HER? *ACS Energy Lett.* **2021**, *6* (4), 1175−1180.

(56) Yu, Q.; Zhang, Z.; Liu, H.; Kang, X.; Ge, S.; Li, S.; Gan, L.; Liu, B. Why Do Platinum Catalysts Show Diverse Electrocatalytic Performance? *Fundam. Res.* **2023**, *3* (5), 804−808.

(57) Ma, W.; Zhang, X.; Li, W.; Jiao, M.; Zhang, L.; Ma, R.; Zhou, Z. Advanced Pt-Based Electrocatalysts for the Hydrogen Evolution Reaction in Alkaline Medium. *Nanoscale* **2023**, *15*, 11759−11776.

(58) Ren, X.; Lin, C.; Zhou, G.; He, J.; Tong, Y.; Chen, P. Pt-Decorated Spinel MnCo$_2$O$_4$ Nanosheets Enable Ampere-Level Hydrazine Assisted Water Electrolysis. *J. Colloid Interface Sci.* **2024**, *676*, 13−21.

(59) Barlow, J. M.; Ziller, J. W.; Yang, J. Y. Inhibiting the Hydrogen Evolution Reaction (HER) with Proximal Cations: A Strategy for Promoting Selective Electrocatalytic Reduction. *ACS Catal.* **2021**, *11* (13), 8155−8164.

(60) Cadle, S. H.; Bruckenstein, S. Inhibition of Hydrogen Adsorption by Submonolayer Deposition of Metals on Platinum. *Anal. Chem.* **1971**, *43* (13), 1858−1862.

(61) Kotz, E. R.; Stucki, S. Ruthenium Dioxide as a Hydrogen-Evolving Cathode. *J. Appl. Electrochem.* **1987**, *17*, 1190−1197.

(62) Campbell, A. L.; Mangan, S.; Ellis, R. P.; Lewis, C. Ocean Acidification Increases Copper Toxicity to the Early Life History Stages of the Polychaete Arenicola Marina in Artificial Seawater. *Environ. Sci. Technol.* **2014**, *48* (16), 9745−9753.

(63) Leal, P. P.; Hurd, C. L.; Sander, S. G.; Armstrong, E.; Fernandez, P. A.; Suhrhoff, T. J.; Roleda, M. Y. Copper Pollution Exacerbates the Effects of Ocean Acidification and Warming on Kelp Microscopic Early Life Stages. *Sci. Rep.* **2018**, *8* (1), 14763.

(64) Bowles, B. J. Formation of Monolayers of Copper on Platinum Electrodes. *Electrochim. Acta* **1970**, *15* (4), 589−598.

(65) Breiter, M. W. Chemisorption of Copper Atoms on Platinized Platinum in Sulphuric Acid Solution. *Trans. Faraday Soc.* **1969**, *65*, 2197−2205.

(66) Tran, T. D.; Nguyen, M. T. T.; Le, H. V.; Nguyen, D. N.; Truong, Q. D.; Tran, P. D. Gold Nanoparticles as an Outstanding Catalyst for the Hydrogen Evolution Reaction. *Chem. Commun.* **2018**, *54*, 3363−3366.

(67) Dimitratos, N.; Vilé, G.; Albonetti, S.; Cavani, F.; Fiorio, J.; López, N.; Rossi, L. M.; Wojcieszak, R. Strategies to Improve Hydrogen Activation on Gold Catalysts. *Nat. Rev. Chem.* **2024**, *8*, 195−210.

(68) Doniach, S.; Sunjic, M. Many-Electron Singularity in X-Ray Photoemission and X-Ray Line Spectra from Metals. *J. Phys. C: Solid State Phys.* **1970**, *3*, 285−291.

(69) Scofield, J. H. Hartree-Slater Subshell Photoionization Cross-Sections at 1254 and 1487 eV. *J. Electron Spectrosc. Relat. Phenom.* **1976**, *8*, 129−137.

(70) Seah, M. P. Simple Universal Curve for the Energy-Dependent Electron Attenuation Length for All Materials. *Surf. Interface Anal.* **2012**, *44* (10), 1353−1359.

(71) Fairley, N.; Fernandez, V.; Richard-Plouet, M.; Guillot-Deudon, C.; Walton, J.; Smith, E.; Flahaut, D.; Greiner, M.; Biesinger, M.; Tougaard, S.; Morgan, D.; Baltrusaitis, J. Systematic and Collaborative Approach to Problem Solving using X-Ray Photoelectron Spectroscopy. *Appl. Surf. Sci. Adv.* **2021**, *5*, No. 100112.

(72) Shirley, D. A. High-Resolution X-Ray Photoemission Spectrum of the Valence Bands of Gold. *Phys. Rev. B* **1972**, *5* (12), 4709.

(73) Fernandez, V.; Kiani, D.; Fairley, N.; Felpin, F.-X.; Baltrusaitis, J. Curve Fitting Complex X-Ray Photoelectron Spectra of Graphite-Supported Copper Nanoparticles using Informed Line Shapes. *Appl. Surf. Sci.* **2020**, *505*, No. 143841.